RSC Advances

PAPER

View Article Online
View Journal | View Issue

Check for updates

Cite this: *RSC Adv.*, 2021, **11**, 7305

Rapid structural regulation, apatite-inducing mechanism and *in vivo* investigation of microwave-assisted hydrothermally treated titania coating†

Lin Chen,‡[a] Junyu Ren,‡[b] Narisu Hu,*[b] Qing Du*[cde] and Daqing Wei *[cde]

Owing to the poor bioactivity of microarc oxidation (MAO) coating and the rapid activation ability of the microwave hydrothermal (MH) technique, MH treatment was applied to optimize the *in vivo* interface status between MAO-treated titanium and bone. In this study, consequently, new outermost layers were prepared using hydroxyapatite (HA) nanorods, HA submicron pillars or sodium titanate nanosheets. The results revealed that the NaOH concentration significantly influenced the surface structure and phase constitution of the MAO samples. Moreover, on enhancing the NaOH concentration, the number of HA phases was decreased. Further, the influence of the NaOH concentration on the interfacial bonding strength was insignificant for concentrations ≤0.5 mol L^{-1}. Transmission electron microscopy (TEM) analysis showed that the induction of apatite was accompanied by the dissolution of the HA crystals and there was excellent crystallographic matching with the HA crystals. The *in vitro* and *in vivo* analyses revealed that the MH-treated MAO sample with the HA nanorods possessed superior apatite-formation ability and osseointegration, including a small amount of soft tissue and optimal bone–implant interfacial bonding force, thus signifying strong potential for the optimization of the bone–implant interfacial status.

Received 6th October 2020
Accepted 25th January 2021

DOI: 10.1039/d0ra08511a

rsc.li/rsc-advances

Open Access Article. Published on 12 February 2021. Downloaded on 1/22/2026 6:37:11 AM.
This article is licensed under a Creative Commons Attribution-NonCommercial 3.0 Unported Licence.

1. Introduction

Titanium (Ti) possesses many advantages among biomedical materials, such as excellent biological activity and biomechanical properties. However, Ti implants suffer from poor bioactivity. Thus, Ti implants cannot be directly connected to bone tissue, and cannot form high interfacial bonding strength, which results in the formation of a poor osseointegration interface and loosening of the implant at the interface.[1,2] Moreover, the osseointegration of titanium implants is mainly influenced by the surface properties, such as topological structure,[3–8] chemistry,[9–12] roughness,[13,14] surface energy/charge[15] and wettability.[15] As a result, various surface treatment technologies have been explored to adjust the surface structure, as well as chemical and physical characteristics, of titanium, such as electrochemical deposition,[16–19] sol–gel method,[20–23] and microarc oxidation (MAO).[24,25] Among the various surface modification methods, MAO represents a relatively effective and rapid method to fabricate TiO_2-based coatings on the titanium surface,[26–30] which can be used to fabricate different functional layers with porous topological structures on the surface within a short treatment time,[29,31–33] as per the requirements and design purpose.

Natural teeth are composed of inorganic hydroxyapatite (HA) crystals, with optimal osteoconductivity and osteoinductivity.[34,35] Previous studies in the literature have reported the effectiveness of hydrothermal treatment (HT)[36–39] for preparing HA crystals on coatings. However, it is very difficult to rapidly fabricate numerous HA phases on the sample surface within a short treatment duration. Our previous studies[40,41] have reported the use of microwave hydrothermal (MH) treatment for effective and rapid surface modification, which accelerates the formation of HA rods on the samples. In addition, the *in vivo* osseointegration of two different structures has been comparatively investigated, indicating that the composite structure with the HA rods/$Na_{0.23}TiO_2$ nanoflakes possesses superior osseointegration ability compared to the structure with just $Na_{0.23}TiO_2$ nanoflakes. Moreover, the Ti–OH group from the exchange of the $Na_{0.23}TiO_2$ with the H_2O significantly promoted the *in vitro* apatite-inducing ability and *in vivo* osseointegration ability.

[a]*Orthopedics, Second Affiliated Hospital of Harbin Medical University, Harbin 150086, China*

[b]*Oral Implant Center, Second Affiliated Hospital of Harbin Medical University, No. 246 Xuefu Road, Nangang District, Harbin 150086, China. E-mail: 56506075@qq.com*

[c]*Center of Analysis and Measurement, Harbin Institute of Technology, Science Park, No. 2 Yikuang Street, Harbin, 150001, China. E-mail: daqingwei@hit.edu.cn; duqing@hit.edu.cn*

[d]*Institute for Advanced Ceramics, Department of Materials Science and Engineering, Harbin Institute of Technology, Harbin, 150001, China*

[e]*Key Laboratory of Advanced Structural-Functional Integration Materials & Green Manufacturing Technology, Harbin Institute of Technology, Harbin, 150001, China*

† Electronic supplementary information (ESI) available. See DOI: 10.1039/d0ra08511a

‡ Lin Chen and Junyu Ren contributed equally to this work.

© 2021 The Author(s). Published by the Royal Society of Chemistry

Open Access Article. Published on 12 February 2021. Downloaded on 1/22/2026 6:37:11 AM.
This article is licensed under a Creative Commons Attribution-NonCommercial 3.0 Unported Licence.

However, it was not clear that the increase in the *in vitro* and *in vivo* inducing ability was due to the HA nanorods or the $Na_{0.23}TiO_2$ nanoflakes. To study it further, three different micro-/nano-scale composite structures (HA nanorods, HA submicron pillars/$Na_{0.23}TiO_2$ nanoflakes and $Na_{0.23}TiO_2$ nanoflakes) were designed in this study. Moreover, the influence of the NaOH concentration on the aspect ratio of the HA rods and the interfacial bonding strength of the MAO coating was systemically investigated. In addition, the apatite-inducing ability and *in vivo* osseointegration phenomena were also studied.

2. Materials and methods

2.1 Specimen fabrication

The Ti sheets (TA2, $10 \times 10 \times 1$ mm^3, *in vitro*) and Ti rods (TA2, $\phi 2 \times 6$ mm^3, *in vivo*) were mechanically treated using 400 and 800 grit abrasive paper. Subsequently, the Ti sheets and Ti rods were treated using microarc oxidation to achieve the Ca–P-incorporated MAO coating, which was labeled as MAO. The details of the MAO treatment process have been reported in our previous studies.[40–42]

For the MH treatment, the MAO specimens were treated in a reaction kettle containing 40 mL of different concentrations of NaOH solution, followed by microwave hydrothermal treatment at 200 °C for 10 min (XH-800S, Beijing Xianghu Science and Technology Development Co., China). During the MH treatment process, the microwave frequency and power were set to 2450 MHz and 800 W, respectively. As for the MH instrument, the microwave power could be continuously adjusted from 1 to 1000 W. Moreover, the maximum temperature and pressure for the MH treatment were 260 °C and 6 MPa, respectively. The reactive temperature and pressure in the autoclave could be monitored in real-time by the computer system. The specimen codes and MH modification parameters are displayed in Table 1.

2.2 Specimen characterization

The phase constitution and surface structure of the MAO- and MH-treated specimens were analyzed using X-ray diffraction (XRD, Empyrean, PANalytical) and scanning electron microscopy equipped with energy-dispersive X-ray spectroscopy (SEM, EDS, Helios Nanolab 600i, FEI Co., USA). The microstructures of the HA nanorods and $Na_{0.23}TiO_2$ nanosheets and MAOMH05 sample after SBF immersion were further studied *via* transmission electron microscopy (TEM, Talos F200X, FEI Co., USA).

Table 1 The parameters and specimen codes for the MH modification process

Specimen code	Temperature (°C)	Electrolyte	Concentration (mol L^{-1})	Time (min)
MAOMH001	200	NaOH	0.01	10
MAOMH05			0.5	
MAOMH3			3.0	

The interfacial adhesion strength of the MAO- and MH-modified samples was measured using the direct pull-off approach. The interfacial adhesion force between the bone and implant was measured using a universal testing machine (Instron 1195, Instron Co., USA). The details of the measurement procedure have been reported in our previous works.[35]

The *in vitro* mineralization test (SBF immersion test) was used to analyze the *in vitro* bioactivity of the modified MAO specimens. Details of the composition of the SBF solution were reported in our previous study.[40]

2.3 *In vivo* animal testing

In this study, all the implantation surgeries fulfilled the requirements of the Animal Care and Experiment Committee. The implantation procedure and analysis approach have already been reported in our previous study.[41] Twelve healthy and mature white rabbits (New Zealand, 2.5–3 kg) were employed for the animal investigation. Four and three implant holes ($\phi 2 \times 6$ mm^3) were made in the left and right tibias for implanting the Ti, MAO, MAOMH001 and MAOMH3 as well as Ti, MAO and MAOMH05 implants, respectively. The interfacial bonding status was evaluated using X-ray digital photography (DHF-155HII, Hitachi, Japan), micro-computed tomography (Micro-CT, Siemens, Siemens Co., USA), VG stained histological analysis, SEM and EDS analyses, and bone–implant contact (BIC%) calculations. Subsequently, the 3D structures of the tibias containing the samples were rebuilt within the distance range $\phi 2 \times 6$ mm^3 to $\phi 3 \times 6$ mm^3 using MINICS 20 (Materialise Co., Belgium).

2.4 Statistical analysis

The bone–specimen interfacial bonding strength and coating-substrate interfacial adhesion strength for the MAO- and MH-treated specimens were measured at least thrice using SPSS software, where a p-value of <0.05 indicated the statistical significance of the results.

3. Results

3.1 Structure and phase constitution of MAO- and MH-treated samples

The effect of the NaOH concentration on the phase constitution and surface structure of the MH-treated MAO samples was studied, as illustrated in Fig. 1. Numerous crater-like micropores with size ranging between 1 and 3 μm were observed on the MAO sample (Fig. 1(a and b)). In the MH-treated MAO samples, the porous structure was observed to be similar to the MAO sample, however, the size of the micropores was smaller. In the case of the MAOMH001 sample, numerous HA nanorods were formed with an average diameter of 100 nm (Fig. 1(c and d)). In the MAOMH05 sample (Fig. 1(e and f)), abundant HA submicron pillars with a diameter of ~200–300 nm were formed. For the NaOH concentration of 3.0 mol L^{-1}, the majority of the HA submicron pillars disappeared from the MAOMH3 sample. Furthermore, large numbers of sodium

© 2021 The Author(s). Published by the Royal Society of Chemistry

Open Access Article. Published on 12 February 2021. Downloaded on 1/22/2026 6:37:11 AM.
This article is licensed under a Creative Commons Attribution-NonCommercial 3.0 Unported Licence.

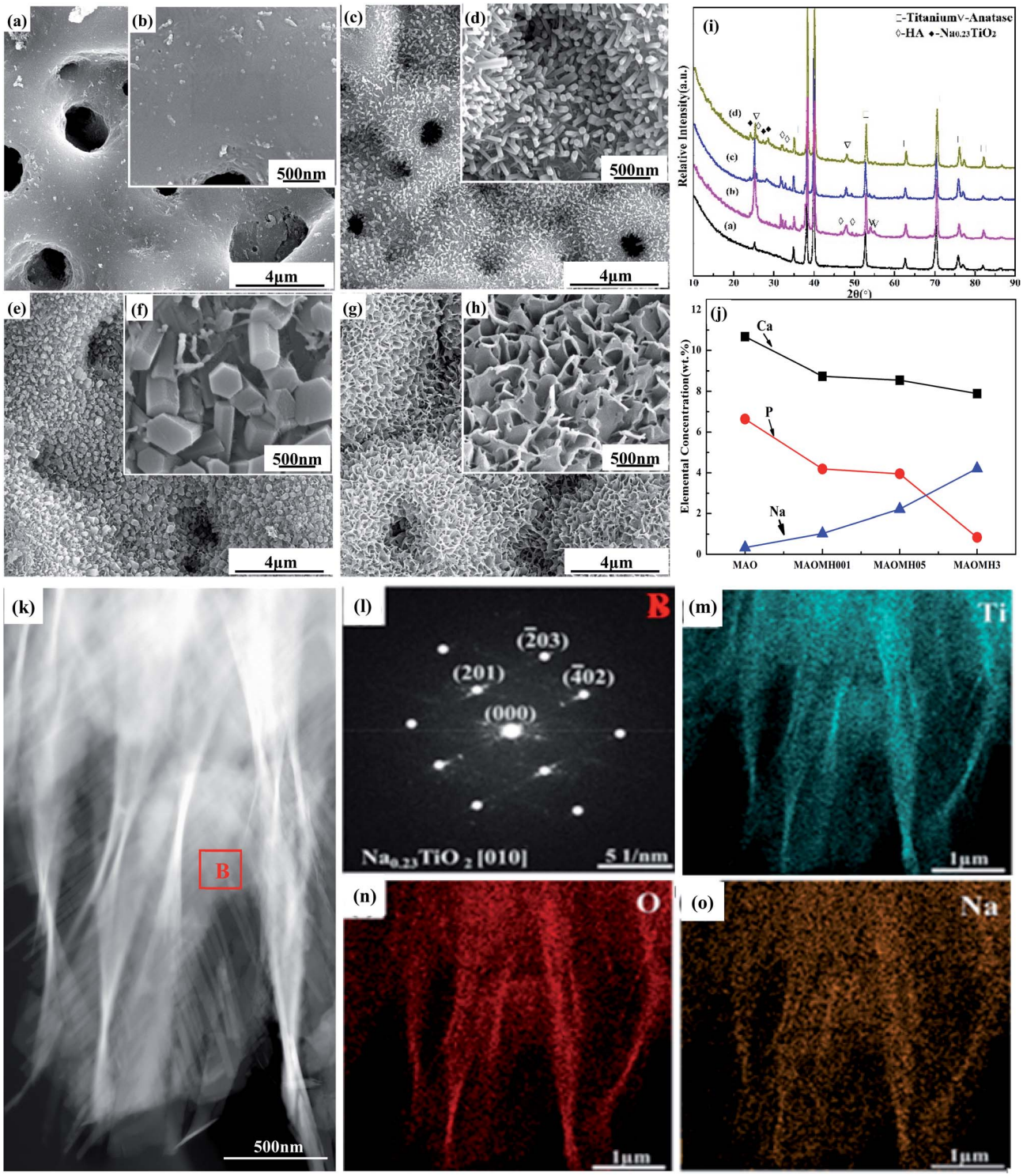

Fig. 1 (a–j) SEM images, XRD patterns, and elemental compositions of (a and b) MAO, (c and d) MAOMH001, (e and f) MAOMH05, and (g and h) MAOMH3. (k–o) TEM images and element mapping distribution for MAOMH3 sample.

titanate ($Na_{0.23}TiO_2$) nanosheets were also observed on the MAOMH3 sample (Fig. 1(g and h)).

As illustrated in Fig. 1(i), the diffraction peaks at $2\theta = 25.1°$, 48.2°, 53.8° and 55.1° were attributed to the anatase phase in the MAO- and MH-treated sample. For the MH-treated MAO samples, the intensities of the anatase diffraction peaks were obviously increased. However, the anatase diffraction intensities were observed to decrease with increasing NaOH concentration from 0.5 to 3 mol L^{-1}. Meanwhile, the diffraction peaks corresponding to HA at $2\theta = 25.8°$, 31.6°, 32.7°, 34.1°, 46.7° and

Open Access Article. Published on 12 February 2021. Downloaded on 1/22/2026 6:37:11 AM.
This article is licensed under a Creative Commons Attribution-NonCommercial 3.0 Unported Licence.

49.5° were detected in the MH-treated samples, where the intensities decreased with increasing NaOH concentration. In addition, a new $Na_{0.23}TiO_2$ phase was detected in the XRD patterns of the MAOMH05 and MAOMH3 samples with its intensity increasing with the NaOH concentration.

The elemental constitution of the MAO- and MH-treated samples is depicted in Fig. 1(j). Comparing with the MAO sample, it was noted that the content of Ca and P elements slightly reduced, while that of Na continuously increased with increasing NaOH concentration. However, the P content sharply reduced on increasing the NaOH concentration to 3.0 mol L^{-1}.

Fig. 1(k) presents the high-angle annular dark field (HAADF) image of the $Na_{0.23}TiO_2$ nanosheets, with its SAED pattern shown in Fig. 4(l), corresponding to the [010] zone axis of the $Na_{0.23}TiO_2$ crystal. Further, the EDS analysis indicated that the $Na_{0.23}TiO_2$ nanosheets mainly consisted of Ti, O and Na elements (Fig. 4(m–o)).

3.2 Interfacial bonding strength

Fig. 2 displays the interfacial adhesion strength of the coatings formed on the Ti substrate. The interfacial adhesion strengths for the MAO, MAOMH001 and MAOMH05 samples were noted to be similar, reaching up to 47.5 MPa, while the strength of the MAOMH3 sample decreased. This indicated that, for the NaOH concentration ≤0.5 mol L^{-1} and 10 min treatment time, the NaOH concentration did not significantly influence the interfacial adhesion strength.

3.3 *In vitro* mineralization tests

The SEM micrographs of the Ti, MAO, and MH-modified MAO samples after SBF soaking for different durations are depicted in Fig. 3. Among the samples, the apatite deposition was first observed on the MAOMH001 sample as the soaking time reached 20 h. However, as the immersion time was further enhanced to 24 h, deposited apatite was also observed on the MAOMH05 sample, with no new deposition observed on MAOMH3. On further extending the soaking duration to 72 h, a large amount of apatite deposition occurred on the MAOMH001 and MAOMH05 samples, with a small amount of deposition on the MAOMH3 sample. Thus, the *in vitro* mineralization ability followed the sequence: MAOMH001 > MAOMH05 > MAOMH3.

In order to further analyze the microstructure of the MAOMH05 sample after SBF immersion for 72 h, a thin slice of the SBF-soaked sample was prepared by FIB, and its microstructure was studied by TEM, as depicted in Fig. 4. As observed in the EDS images (Fig. 4(b–e)), four typical regions could be identified in the cross-section of the SBF-soaked MAOMH05 sample, denoted as A, B, C and D. It was noted that the concentrations of Ca, O and P in region B were higher than those in region A. Moreover, based on the typical apatite structure (Fig. 3) and elemental composition (Fig. 4), the outermost deposited layer was determined to be apatite. Moreover, the HA nanorods were still observed in their entirety even after SBF soaking for 72 h. Regions C and D were observed in the inner coating, and region C was situated near the outermost layer. Thus, region C consisted of Ti and O elements, with a small amount of Ca and P, which were lower than those in region D.

The SAED and HRTEM images in Fig. 4(g–i) show that the diffraction spots and microstructure were retained, thus suggesting that the HA nanorods still existed after SBF soaking. A few diffraction spots corresponding to the (002) and (211) crystal planes were observed in the SAED image of apatite, thus exhibiting poor crystallinity of the deposited apatite. In Fig. 4(i), the *d*-spacing values of 0.344 nm and 0.282 nm correspond to the (002) and (211) crystal planes of apatite, whereas the *d*-spacing values of 0.688 nm and 0.817 nm conferred with the (001) and (100) crystal planes of the HA phase, thus showing that the deposited apatite had excellent crystallographic matching with HA. In addition, the interface layer with a width of 1.3 nm between HA and apatite was also observed in the high-resolution TEM image. Its microstructure was not complete, which indicated that the formation of apatite was accompanied by the dissolution of the HA nanorods.

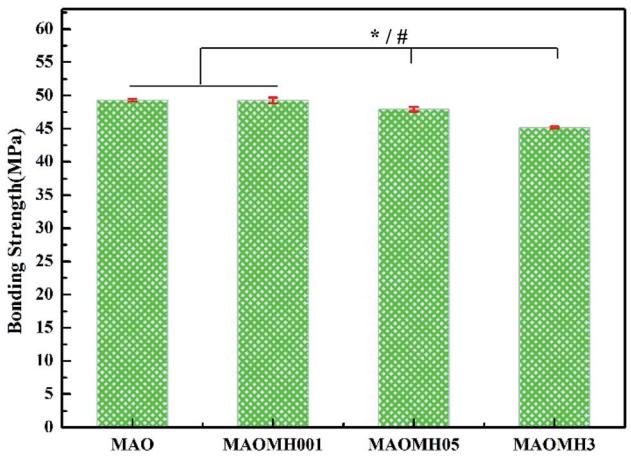

Fig. 2 The interfacial adhesion strengths of the MAO, MAOMH001, MAOMH05 and MAOMH3 samples. * refers to the comparison between MAO, MAOMH001, MAOMH05 and MAOMH3 ($p < 0.05$) and # refers to the comparison between MAOMH001, MAOMH05 and MAOMH3 ($p < 0.05$).

3.4 *In vivo* osseointegration evaluation

3.4.1 X-ray analysis. X-ray diffraction represents an effective method to evaluate the interfacial bonding status. Fig. 5 presents the typical X-ray radiographs of the tibia containing the Ti, MAO, MAOMH001, MAOMH05 and MAOMH3 samples after healing for 16 weeks. As illustrated in Fig. 5(a and b), the interfacial status between the Ti, MAO, MAOMH001, MAOMH05 and MAOMH3 samples and bone was noted to be optimal. Further, the samples remained at the original implantation site in the tibia, and no fracture phenomenon of the tibia around the Ti, MAO, MAOMH001, MAOMH05 and MAOMH3 samples was noted, even though the tibia containing the modified titanium implant was under load.

3.4.2 Micro-CT observation. Fig. 6 shows the micro-CT colorized coronal and sagittal viewing images of the tibia

© 2021 The Author(s). Published by the Royal Society of Chemistry

Open Access Article. Published on 12 February 2021. Downloaded on 1/22/2026 6:37:11 AM.
This article is licensed under a Creative Commons Attribution-NonCommercial 3.0 Unported Licence.

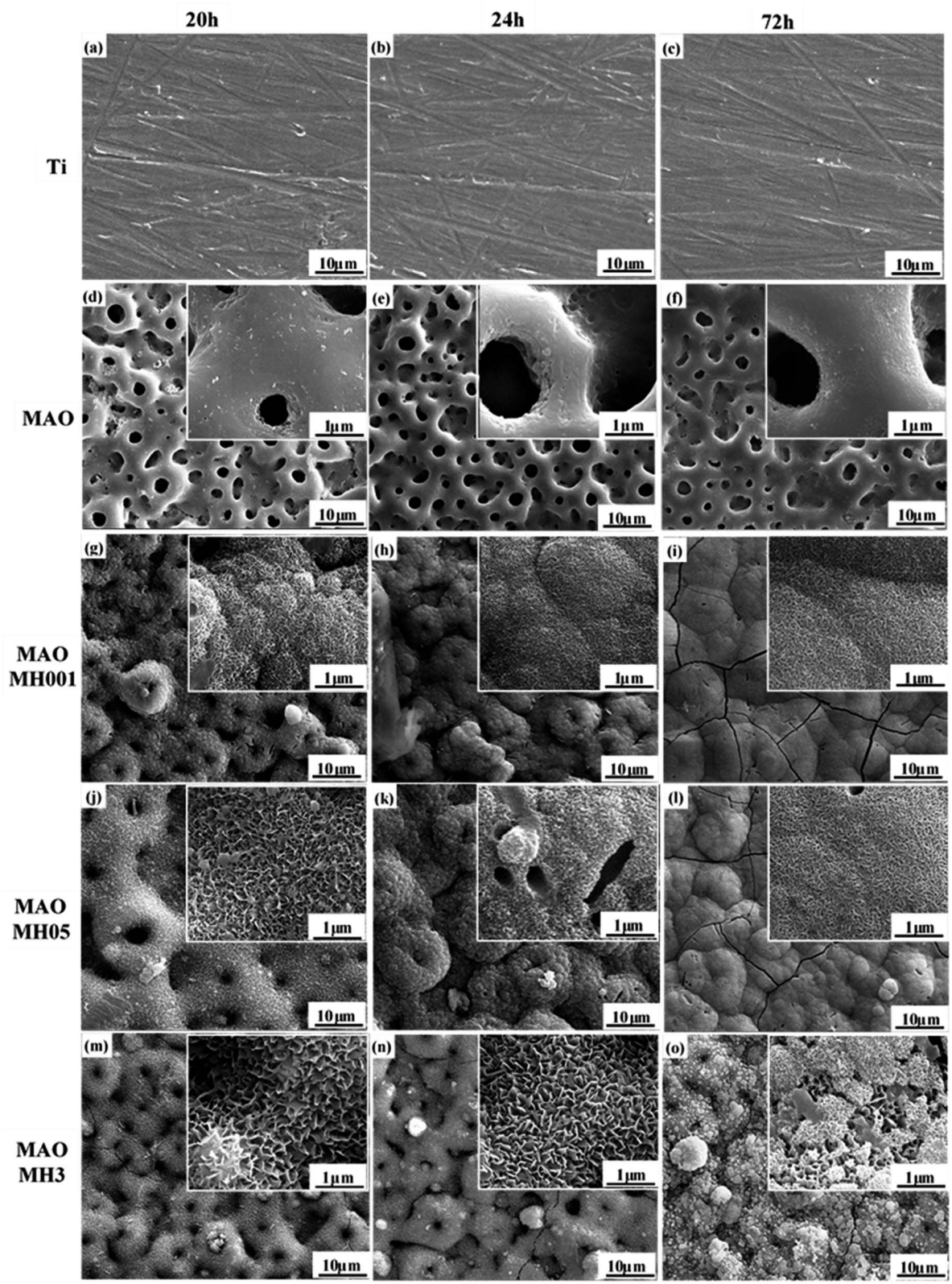

Fig. 3 SEM micrographs of Ti, MAO and MH-treated MAO samples after SBF soaking for 20, 24 and 72 h: (a–c) Ti, (d–f) MAO, (g–i) MAOMH001, (j–l) MAOMH05, and (m–o) MAOMH3.

Open Access Article. Published on 12 February 2021. Downloaded on 1/22/2026 6:37:11 AM.
This article is licensed under a Creative Commons Attribution-NonCommercial 3.0 Unported Licence.

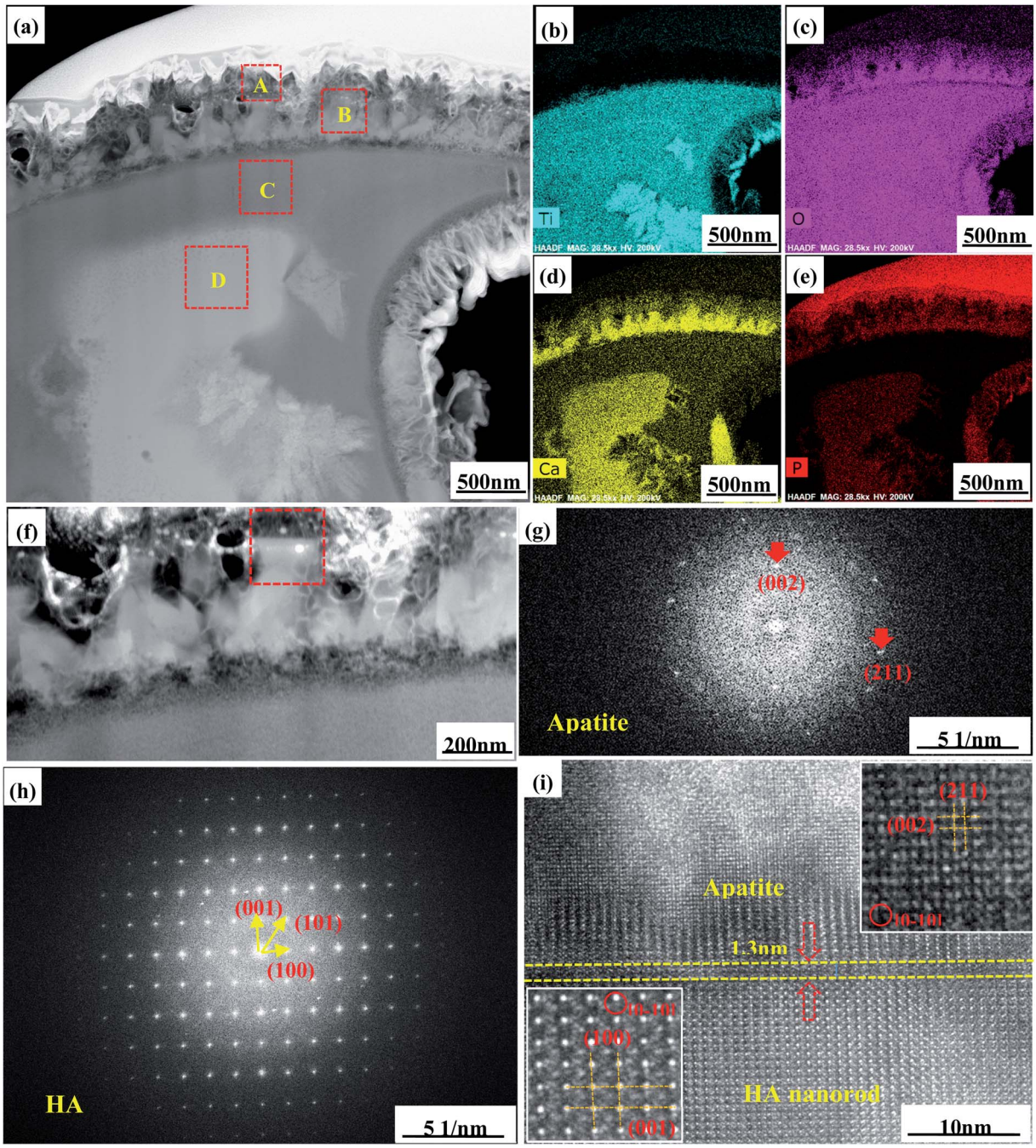

Fig. 4 Cross-sectional TEM images (a and f), SAED patterns (g and h), HRTEM images (i) and EDS mapping results (b–e) for the MAOMH05 sample after soaking in SBF for 72 h.

containing the Ti, MAO, MAOMH001, MAOMH05 and MAOMH3 samples after healing for 16 weeks. In these images, the bone tissue displays green, soft tissue displays light red and the implants present as blue owing to the variations in the X-ray absorption ability.

The implants were observed to have a strong connection with the bone tissue. The small amounts of fibrous tissue marked by the white arrows exhibited the continuous connection with the Ti and MAO implants from the coronal and sagittal viewing directions (Fig. 6(a, b, f and g)). The amount of soft tissue surrounding the MAOMH001, MAOMH05 and MAOMH3 implants was obviously decreased, which indicated the point-like contact with the implants. Meanwhile, the surface of the MAOMH001 and MAOMH05 implants showed continuous contact with the bone tissue from the coronal and sagittal viewing directions. In addition, no obvious fracture was noted at the interface of the MAOMH001 and MAOMH05 implants with the bone material. Therefore, an excellent interface status could be confirmed between the MAOMH001 and MAOMH05 samples and the bone material.

© 2021 The Author(s). Published by the Royal Society of Chemistry

Open Access Article. Published on 12 February 2021. Downloaded on 1/22/2026 6:37:11 AM.
This article is licensed under a Creative Commons Attribution-NonCommercial 3.0 Unported Licence.

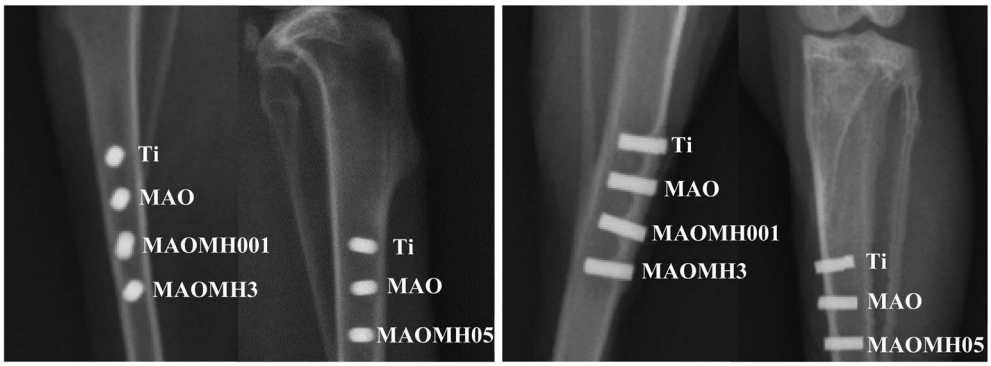

Fig. 5 X-ray images for the tibias containing the Ti, MAO, MAOMH001, MAOMH05 and MAOMH3 specimens after healing for 16 weeks.

3.4.3 Hard histological analysis. Fig. 7 shows the histological images for the biological tissue surrounding the samples at the cortical region after healing for 16 weeks. After 6 weeks, new bone tissue was observed to be formed in the cortical regions (Fig. 7(a–e)). However, the amount of soft tissue (marked as the white arrows) surrounding the MH-modified MAO sample was less than the tissue surrounding the Ti and MAO implant–bone interface. Moreover, new bone tissue was noted to be formed on the MH-treated MAO samples at the bone marrow cavity parts (shown in Fig. S4†). The magnified image in Fig. 7(f) revealed that the majority of the new bone surrounding the Ti implant was separated by soft tissue (marked as the white arrow), thus preventing a direct connection with the bone. For the MAO sample, the majority of the new bone was indirectly connected with the MAO sample through the formed osteoid, while a part of the new bone was separated by the fibrous tissue surrounding the MAO sample (Fig. 7(g)). As shown in the magnified histological images (Fig. 7(h–j)), the MH-treated MAO samples exhibited excellent direct connection with the bone material at the cortical regions. However, a small amount of fibrous tissue was also seen around the MH-modified MAO samples, as illustrated in Fig. 7(c–e). In addition, the extent of the fibrous tissue around MAOMH001, MAOMH05 and MAOMH3 followed the sequence: MAOMH001 < MAOMH05 < MAOMH3. The observed findings were verified by the bone–implant contact (BIC%) analysis, as shown in Fig. 7(k). The BIC% of the MH-modified MAO samples was observed to be larger than that of the Ti and MAO implants, especially

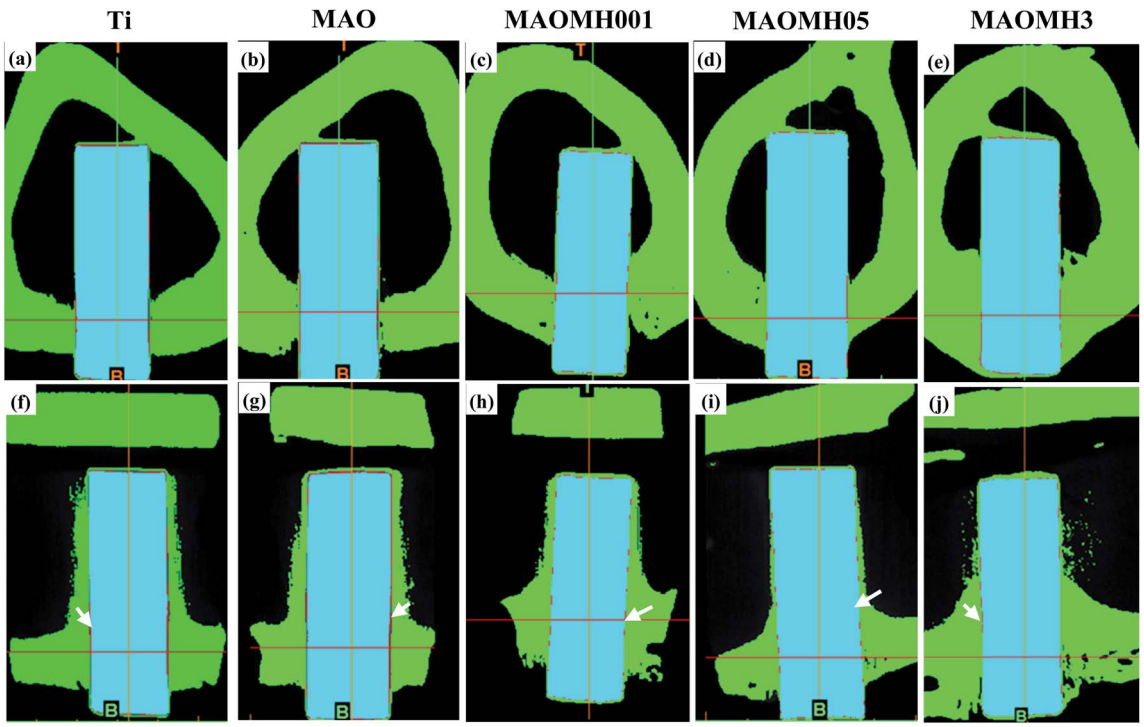

Fig. 6 The micro-CT-colorized coronal and sagittal viewing photographs for the tibias containing the Ti (a and f), MAO (b and g), MAOMH001 (c and h), MAOMH05 (d and i) and MAOMH3 (e and j) specimens after healing for 16 weeks. Note: the fibrous tissues are marked by white arrows.

Open Access Article. Published on 12 February 2021. Downloaded on 1/22/2026 6:37:11 AM.
This article is licensed under a Creative Commons Attribution-NonCommercial 3.0 Unported Licence.

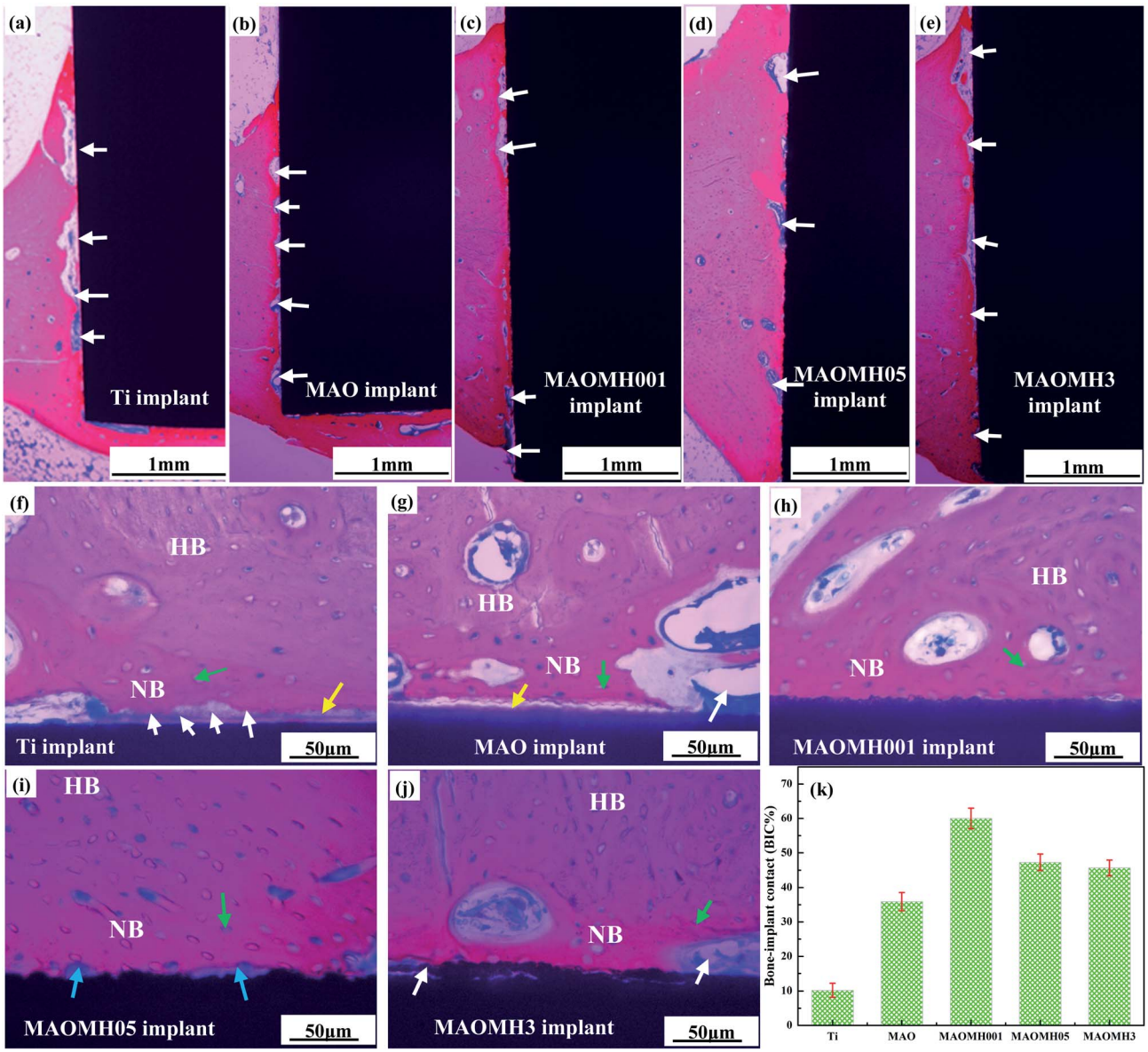

Fig. 7 Histological images of the biological tissues surrounding the samples at the cortical regions after healing for 16 weeks: (a and f) Ti, (b and g) MAO, (c and h) MAOMH001, (d and i) MAOMH05, (e and j) MAOMH3, (k) the BIC%. Note: NB represents new bone, HB represents host bone, yellow arrow represents osteoid, white arrow represents fibrous tissues, green arrow represents osteocytes and blue arrow represents osteoblasts.

MAOMH001, which was in agreement with the findings from the histological analysis.

3.4.4 Biological mechanical analysis and surface structure of implants after pushing out. Fig. 8 depicts the pushing out force and surface structure of the Ti, MAO, MAOMH001, MAOMH05 and MAOMH3 samples pushing out from the tibias after healing for 16 weeks. As depicted in Fig. 8(a), for the Ti sample, the pushing out force was about 15 N, while it was about 60 N for MAO, indicating a four-fold increment. Further, the pushing out force for the MAOMH001, MAOMH05 and MAOMH3 samples exhibited greater improvements compared with the MAO sample. In particular, for MAOMH001 and MAOMH05, the pushing out force values were about 145 and 126 N, increasing by 2.5- and 2-fold, respectively, as compared with the MAO sample. Thus, the pushing out forces could be ranked as MAOMH001 > MAOMH05 > MAOMH3 > MAO > Ti.

The SEM micrographs of the Ti, MAO, MAOMH001, MAOMH05 and MAOMH3 samples after being pushing out from the tibias are presented in Fig. 8(b–f). The SEM images confirmed the presence of residual biological tissue on the implants. The Ti implant exhibited poor contact with the bone (Fig. 8(b)), and EDS results suggested that the residual biological tissue mainly comprised soft tissue (C 50.04 at% and Ca 5.48 at%). Compared to the Ti implant, a higher amount of soft tissue (as shown by the yellow arrow) and osteoblast cells (as marked by the red arrow) was also observed on the MAO

© 2021 The Author(s). Published by the Royal Society of Chemistry

Open Access Article. Published on 12 February 2021. Downloaded on 1/22/2026 6:37:11 AM.
This article is licensed under a Creative Commons Attribution-NonCommercial 3.0 Unported Licence.

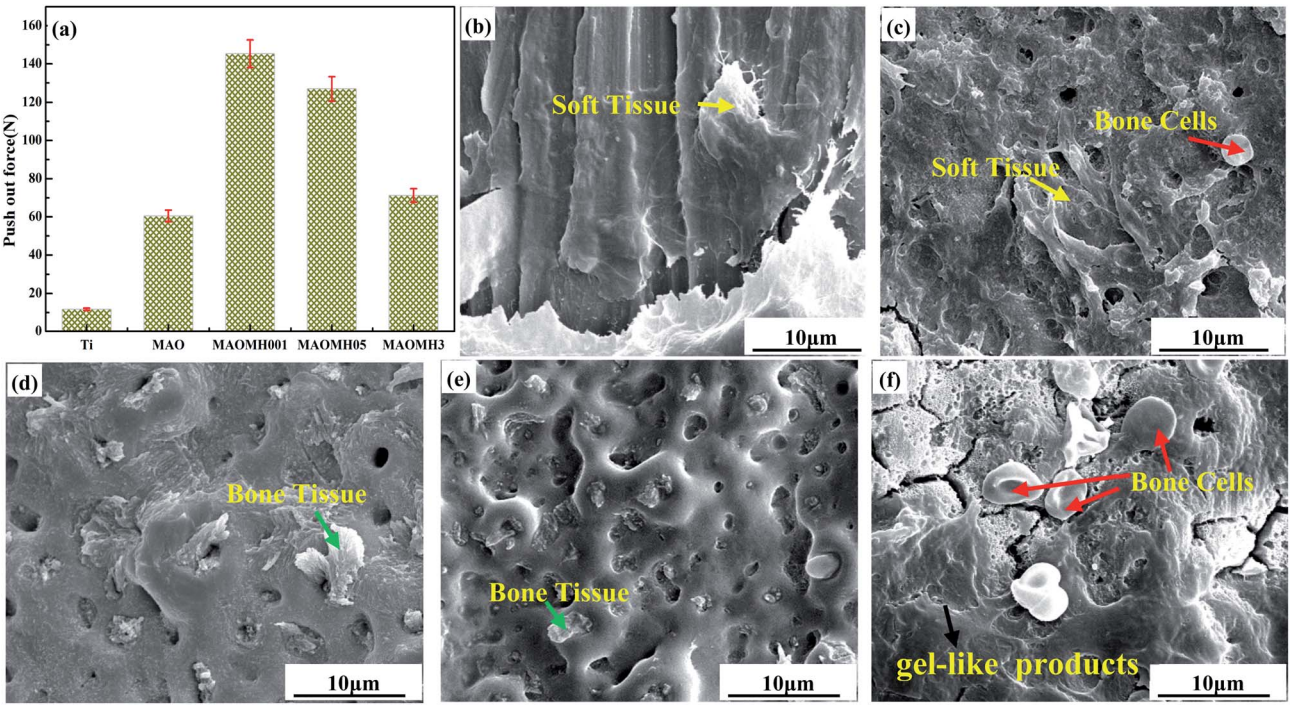

Fig. 8 Push-out force (a) and SEM micrographs for the Ti (b), MAO (c), MAOMH001 (d), MAOMH05 (e) and MAOMH3 (f) samples taken out from the tibia after healing for 16 weeks.

implant (Fig. 8(c)). Further, the porous structure was retained after pushing out, thus, suggesting that the fracture took place at the bone tissue side. In the MAOMH001 implant (Fig. 8(d)), a large amount of bone tissue (as marked by the green arrow) (Ca 16.82 at% and P 6.02 at%) grew into the micropores on the MAOMH001 implant, and a small amount of fibrous tissue was observed on the surface. In addition, the porous structure was retained, indicating optimal interfacial bonding with the implant. For the MAOMH05 implant, a small amount of bone tissue remained on the sample. At the same time, the MAOMH05 coating was not peeled off, as shown in Fig. 8(e), thus, showing that the fracture took place at the bone site owing to the formation of immature bone (as shown in Fig. 7(i)). As observed in Fig. 8(f), the mineralization deposition of the gel-like products (as marked by the black arrow) and bone cells (as marked by red arrows) were also observed on the pushed-out MAOMH3 implant. The fracture was observed at the bone side, thus suggesting that the mineralization deposition on the MAOMH3 sample did not sustain the load during the pushing-out operation.

4. Discussion

4.1 Microstructure of MH-treated MAO samples

In this study, based on the XRD and SEM analyses (Fig. 1), the MH treatment time and NaOH concentration significantly affected the microstructure of the MH-modified micro arc oxidized coating. After MH modification, the diffraction intensity of the anatase peaks was enhanced in comparison with the MAO sample, which was attributed to the critical atmosphere produced through the MH treatment, thus promoting the crystallization of anatase. Further, the microstructures of the MH-treated MAO samples were compared as a function of the NaOH concentration. During the MH treatment, the high temperature and pressure could enhance the migration ability of the bioactive elements (Ca and P). Thus, the local concentrations of the Ca and P elements were increased, which led to the dissolution into solution to form PO_4^{3-} and Ca^{2+} ions, followed by the subsequent combination with the OH ions to form the HA crystals. On enhancing the NaOH concentration to 0.5 and 3.0 mol L^{-1}, a few HA rods with a small aspect ratio were observed on the MAOMH05 sample, whereas the rods seemed to disappear from the MAOMH3 sample. Further, the amount of HA nanorods on the MAOMH05 and MAOMH3 samples was reduced in comparison with the amount on the MAOMH001 sample. The reason for the observed behavior was as follows: first, the concentration of the bioactive elements (Ca and P) was obviously reduced (Fig. 1). Second, the high temperature, pressure and NaOH concentration significantly enhanced the corrosive nature of the OH ions towards the anatase TiO_2 phase, which significantly damaged the structure of the coating, thus hindering the nucleation of the HA nuclei.

4.2 *In vitro* mineralization and animal analysis of MH-modified MAO samples

4.2.1 *In vitro* apatite-inducing ability. In this study, the MH-modified MAO samples exhibited superior bioactivity as compared to the MAO and pure Ti samples. After soaking in the mineralization solution for 20 h, the MAOMH001 sample was observed to be completely covered with the deposited apatite,

Open Access Article. Published on 12 February 2021. Downloaded on 1/22/2026 6:37:11 AM.
This article is licensed under a Creative Commons Attribution-NonCommercial 3.0 Unported Licence.

which was superior to the MAOMH05 and MAOMH3 samples (Fig. 3), and the HA nanorod array reported earlier by Han.[43] Thus, the apatite-inducing ability of the modified MAO samples followed the sequence: MAOMH001 > MAOMH05 > MAOMH3. The reason for the observed high bioactivity of the MAOMH001 sample was attributed to the formation of the Si–HA nanorods with high crystallinity and degradability. The previous literature study reported that the ionic substituted HA nanorods such as Sr, Si and F ions had higher solubility.[42,43] In addition, the Si-doped HA crystals had higher solubility than the pure HA crystals because the substitution of PO_4^{3-} by SiO_4^{3-} ions could change the crystal structure of the HA phase. Therefore, the Si–HA crystals were easily degraded owing to the formation of the crystal defects after the substitution. Moreover, the Si–HA crystals could provide more Ca^{2+} and PO_4^{3-} near the MAOMH001 sample, thus accelerating the deposition of apatite. Meanwhile, the HA nanorods exhibited effective crystallographic matching with apatite (Fig. 4), which decreased the Gibbs free energy for the apatite nucleation and reduced the formation time for apatite deposits.

Once soaked in the SBF solution, the HA nanorods as well as the enriched content of Ca and P gradually dissolved to release the Ca^{2+} and PO_4^{3-} ions, which enhanced the local content of Ca^{2+} and PO_4^{3-} ions near the outermost layer. It promoted the apatite nucleation, which was verified by the HRTEM image shown in Fig. 4(i). In the case of the SBF solution with pH 7.4, the MAOMH001 sample was noted to be more negatively charged (Fig. S3†), which selectively attracted Ca^{2+} ions to form the Ca^{2+}-rich positively charged surface. Subsequently, the abundant PO_4^{3-} ions were absorbed around the positively charged surface to promote the apatite nucleation. As the soaking time was extended, the apatite nucleation grew continuously by absorbing the PO_4^{3-}, CO_3^{2-} and Ca^{2+} ions from the SBF solution owing to the high supersaturation of the SBF solution with respect to apatite.

4.2.2 *In vivo* osseointegration. In our previous studies,[44–46] both Ti and MAO led to extensive coverage of the implants by soft tissue *in vivo*. Obviously, the production of soft tissue is a signal that the material implant is an alien invasion. Therefore, no soft tissue is formed at the ideal bone–implant interface. Thus, research efforts are focused on optimizing the bioactivity of the MAO sample through rapid surface optimization, thus avoiding the limitations of other surface modification methods, including the loss of the bioactive elements and weak interfacial bonding strength.

Based on studies reported in the literature,[45,47,48] the effective fabrication of HA phase on the titanium implant surface reduces the production of soft tissue at the bone–implant interface. Therefore, in this study, the rapid MH treatment process was developed to promote the formation of a large number of HA rods on the MAO sample. As a result, the MH-treated MAO sample exhibited optimal interfacial adhesion strength, thus preventing the loss of the implant owing to the peeling off of the bioactive coating under load.

The X-ray and micro-CT images revealed the compatibility of the implants *in vivo*. However, the implant–bone contact status could not be established from the micro-CT and X-ray analyses. Thus, histological and SEM analyses were performed to study the status of the interface between the implant and bone. The osseointegration of three different composite structures (nanorods, submicron pillars/nanosheets, nanosheets) was comparatively investigated. After MH modification, the wetting angle, surface energy and surface charge of the MAO samples were noted to be optimized (Fig. S1–S3†). A few literature studies[3–12,15] have reported that the topological structure, chemistry, surface energy/charge and wettability significantly influenced the cell–material interaction, further affecting the *in vivo* osseointegration ability. The micro-scale and nano-scale topological structures have also been proven to markedly affect the osteoblast adhesion, proliferation and other cell behaviors, thus enhancing the integration between the implant and surrounding bone tissue.[49–51] Positively charged protein as the transition layer has been reported to play an important role in the cell–material interaction, significantly affecting the surface energy, negatively charged surface and wettability.[52–54] In this study, the MAOMH001, MAOMH05 and MAOMH3 samples exhibited similar micro/nano-scale structure, surface energy/charge and wettability. The micro/nano double scale surface with high surface energy (>85 mJ m^{-2}), significantly negatively charged surface and superior hydrophilicity enhanced the interaction ability between the osteoblast cells and the modified MAO samples, thus enhancing the osseointegration of the modified samples. However, the chemical composition of the MAOMH001, MAOMH05 and MAOMH3 samples was significantly different (Si–HA nanorods, HA submicron pillars–$Na_{0.23}TiO_2$ nanoflakes and $Na_{0.23}TiO_2$ nanoflakes). Previous literature studies have reported that the HA nanomaterial enhances the osteoblast adhesion ability, thus further promoting the *in vivo* osseointegration ability.[42,43,45] Moreover, the Si-substituted HA crystals can accelerate the expression of the related osteoblast genes, thus, promoting the cell–material interaction ability and improving the *in vivo* interface status.[55,56] Based on the comprehensive factors, the MAOMH001 sample with Si–HA nanorods exhibited excellent osseointegration and *in vivo* interface status. Further, based on the histological images, the MAOMH001 sample displayed a faster rate of formation of new bone tissue as compared to the other materials. Thus, it exhibited superior osseointegration owing to the high apatite-inducing ability. Moreover, a small amount of soft tissue was observed at the interface (Fig. 7(h) and 8). Besides, the MAOMH05 implant also exhibited a high level of osseointegration; however, the pushing-out force for the MAOMH05 sample was smaller than that for the MAOMH001 sample. The main reason for the observed behavior was the low-level apatite-formation ability of the MAOMH05 sample, thus forming immature bone tissue, which could not bear the load. In contrast, the MAOMH3 implant exhibited a minor bone–implant contact owing to the formation of soft tissue (Fig. 7(j)). The fracture behavior of the new bone tissue surrounding the implant mainly relied on the *in vivo* interface status. The biological mechanical analyses indicated that the MAOMH001 sample exhibited a superior *in vivo* interface bonding status as compared with the MAOMH05 and MAOMH3 samples, which was also confirmed by the fracture structure after pushing out the implants. The observed fracture behavior can be described as

© 2021 The Author(s). Published by the Royal Society of Chemistry

Open Access Article. Published on 12 February 2021. Downloaded on 1/22/2026 6:37:11 AM.
This article is licensed under a Creative Commons Attribution-NonCommercial 3.0 Unported Licence.

follows: (I) the fracture sites for MAOMH001 and MAOMH05 samples were situated at the bone side. However, there was more residual new bone tissue on the surface of the pushed-out MAOMH001 sample than that on the MAOMH05 sample, which was attributed to its superior apatite-inducing ability and cell–material interaction ability. (II) After MH treatment, the MAOMH001 sample still exhibited a porous surface, which could lead to the growth of bone tissue in the micropores, thus improving the integration interface status of the implant with the bone tissue. Therefore, under load, the new bone tissue in the micropores was observed to be broken. On the fracture surface of the MAOMH001 and MAOMH05 samples, the as-formed Si–HA nanorods and HA submicron pillars were noted to disappear, indicating their integration with the new bone tissue during the healing process. However, the composite materials containing the HA nanomaterial and bone could not bear the large loads. Interestingly, a small amount of newly formed bone tissue was observed in the MAOMH001 implant at the bone marrow cavity, suggesting that the newly formed modified layer with the HA crystals possessed excellent osteoconductivity and osteoinductivity.[35,36] Likewise, a similar phenomenon was observed for the MAOMH05 sample owing to the formation of the HA submicron pillars. Apart from this, for the top side of the implant situated near the other side of the cortical bone, new bone tissue was also formed on the top of the MAOMH05 and MAOMH3 samples, as compared to the Ti and MAO samples (Fig. S4†). Overall, in this study, the new bone formation mechanism surrounding the MH-treated MAO samples involved distance osteogenesis and contact osteogenesis, which needs to be further investigated in future studies.

5. Conclusion

In this study, an outermost bioactive coating of hydroxyapatite (HA) nanorods or HA submicron pillars or sodium titanate nanosheets was rapidly formed on titanium through MAO and MH modification. The surface micrographs and phase constitution of the MH-treated MAO samples could be adjusted by altering the NaOH concentration. Moreover, the interfacial adhesion strength between the MH-treated MAO coating and the titanium matrix was noted to be strong for NaOH concentrations $\leq$0.5 mol L^{-1} and 10 min treatment duration. TEM analysis revealed that the formation of apatite was accompanied by the dissolution of the HA crystals and there was excellent crystallographic matching with HA. In addition, the *in vitro* and *in vivo* analyses suggested that the MH-treated MAO samples containing HA crystals exhibited superior apatite-formation and osseointegration abilities, especially the MAOMH001 sample, along with a small amount of soft tissue and optimal bone–implant interface bonding, thus confirming the potential of the modified titanium implant in the dental field.

Ethical statement

All animal procedures were performed in accordance with the Guidelines for Care and Use of Laboratory Animals of the Second Affiliated Hospital of Harbin Medical University and approved by the Animal Ethics Committee of the Second Affiliated Hospital of Harbin Medical University.

Conflicts of interest

There are no conflicts to declare.

Acknowledgements

We are thankful for the financial support from the National Natural Science Foundation of China (Grant No. 81771106), the National Natural Science Foundation, Innovation Research Group Natural Fund (Grant No. 51621091), and the National Basic Science Research Program (2012CB933900). Moreover, we would like to express our gratitude to EditSprings (https://www.editsprings.com/) for the professional language editing service provided for this manuscript.

References

1 V. Rani, L. Vinothkumar, V. C. Anitha, *et al.*, Osteointegration of titanium implant is sensitive to specific nanostructure morphology, *Acta Biomater.*, 2012, **8**(5), 1976–1989.
2 L. Zhang and T. J. Webster, Nanotechnology and nanomaterial: promises for improved tissue regeneration, *Nano Today*, 2009, **4**(1), 66–80.
3 S. W. Kuo, H. I. Lin, J. H. Ho, *et al.*, Regulation of the fate of human mesenchymal stem cells by mechanical and stereotopographical cues provided by silicon nanowires, *Biomaterials*, 2012, **33**(20), 5013–5022.
4 J. Liu, X. Wang, Q. Jin, *et al.*, The stimulation of adipose-derived stem cell differentiation and mineralization by ordered rod-like fluorapatite coatings, *Biomaterials*, 2012, **33**(20), 5036–5046.
5 S. Okada, H. Ito, A. Nagai, *et al.*, Adhesion of osteoblast-like cells on nanostructured hydroxyapatite, *Acta Biomater.*, 2010, **6**(2), 591–597.
6 L. Zhao, L. Hu, K. Huo, *et al.*, Mechanism of cell repellence on quasi-aligned nanowire arrays on Ti alloy, *Biomaterials*, 2010, **31**(32), 8341–8349.
7 J. Lee, B. H. Chu, K. H. Chen, *et al.*, Randomly oriented, upright SiO_2 coated nanorods for reduced adhesion of mammalian cells, *Biomaterials*, 2009, **30**(27), 4488–4493.
8 J. K. Park, Y. J. Kim, J. Yeom, *et al.*, The topographic effect of zinc oxide nanoflowers on osteoblast growth and osseointegration, *Adv. Mater.*, 2010, **22**(43), 4857–4861.
9 X. Liu, J. Y. Lim, H. J. Donahue, *et al.*, Influence of substratum surface chemistry/energy and topography on the human fetal osteoblastic cell line hFOB 1.19: phenotypic and genotypic responses observed in vitro, *Biomaterials*, 2007, **28**(31), 4535–4550.
10 S. Heydarkhan-Hagvall, J. M. Gluck, C. Delman, *et al.*, The effect of vitronectin on the differentiation of embryonic stem cells in a 3D culture system, *Biomaterials*, 2012, **33**(7), 2032–2040.

© 2021 The Author(s). Published by the Royal Society of Chemistry

Open Access Article. Published on 12 February 2021. Downloaded on 1/22/2026 6:37:11 AM.
This article is licensed under a Creative Commons Attribution-NonCommercial 3.0 Unported Licence.

11 R. J. Miron, C. J. Oates, A. Molenberg, *et al.*, The effect of enamel matrix proteins on the spreading, proliferation and differentiation of osteoblasts cultured on titanium surfaces, *Biomaterials*, 2010, **31**(3), 449–460.
12 Y. Sugita, K. Ishizaki, F. Iwasa, T. Ueno, H. Minamikawa, M. Yamada, T. Suzuki and T. Ogawa, Effects of pico-to-nanometer-thin TiO_2 coating on the biological properties of micro roughened titanium, *Biomaterials*, 2011, **32**(33), 8374–8384.
13 B. Setzer, M. Bächle, M. C. Metzger, *et al.*, The gene-expression and phenotypic response of hFOB 1.19 osteoblasts to surface-modified titanium and zirconia, *Biomaterials*, 2009, **30**(6), 979–990.
14 A. Dolatshahi-Pirouz, T. Jensen, D. C. Kraft, *et al.*, Fibronectin adsorption, cell adhesion, and proliferation on nanostructured tantalum surfaces, *ACS Nano*, 2010, **4**(5), 2874.
15 J. Y. Lim, M. C. Shaughnessy, Z. Zhou, *et al.*, Surface energy effects on osteoblast spatial growth and mineralization, *Biomaterials*, 2008, **29**(12), 1776–1784.
16 N. N. C. Isa, Y. Mohd and N. Yury, Electrochemical deposition and characterization of hydroxyapatite (HAp) on titanium substrate, *APCBEE Proc.*, 2012, **3**, 46–52.
17 A. Rakngarm and Y. Mutoh, Electrochemical depositions of calcium phosphate film on commercial pure titanium and Ti–6Al–4V in two types of electrolyte at room temperature, *Mater. Sci. Eng., C*, 2009, **29**(1), 275–283.
18 I. Batistić and J. Stojanovski, Electrochemically assisted co-precipitation of protein with calcium phosphate coating on titanium alloy, *Biomaterials*, 2004, **25**(23), 5395–5403.
19 Q. Zhang, Y. Leng and R. Xin, A comparative study of electrochemical deposition and biomimetic deposition of calcium phosphate on porous titanium, *Biomaterials*, 2005, **26**(16), 2857–2865.
20 W. Zhang, W. Liu, Y. Liu, *et al.*, Tribological behaviors of single and dual sol–gel ceramic films on Ti–6Al–4V, *Ceram. Int.*, 2009, **35**(4), 1513–1520.
21 X. X. Wang, S. Hayakawa, K. Tsuru, *et al.*, Bioactive titania gel layers formed by chemical treatment of Ti substrate with a H_2O_2/HCl solution, *Biomaterials*, 2002, **23**(5), 1353–1357.
22 M. F. Hsieh, L. H. Perng and T. S. Chin, Hydroxyapatite coating on Ti6Al4V alloy using a sol–gel derived precursor, *Mater. Chem. Phys.*, 2002, **74**(3), 245–250.
23 E. Milella, F. Cosentino, A. Licciulli, *et al.*, Preparation and characterization of titania/hydroxyapatite composite coatings obtained by sol–gel process, *Biomaterials*, 2001, **22**(11), 1425–1431.
24 C. Wang, F. Wang and Y. Han, The structure, bond strength and apatite-inducing ability of micro-arc oxidized tantalum and their response to annealing, *Appl. Surf. Sci.*, 2016, **361**, 190–198.
25 J. H. Wang, J. Wang, Y. Lu, *et al.*, Effects of single pulse energy on the properties of ceramic coating prepared by micro-arc oxidation on Ti alloy, *Appl. Surf. Sci.*, 2015, **324**, 405–413.
26 E. Matykina, R. Arrabal, P. Skeldon, *et al.*, Transmission electron microscopy of coatings formed by plasma electrolytic oxidation of titanium, *Acta Biomater.*, 2009, **5**(4), 1356–1366.
27 X. He, G. Zhang, X. Wang, *et al.*, Biocompatibility, corrosion resistance and antibacterial activity of TiO_2/CuO coating on titanium, *Ceram. Int.*, 2017, **43**(18), 16185–16195.
28 B. S. Necula, J. P. T. M. V. Leeuwen, L. E. Fratila-Apachitei, *et al.*, In vitro cytotoxicity evaluation of porous TiO_2–Ag antibacterial coatings for human fetal osteoblasts, *Acta Biomater.*, 2012, **8**(11), 4191–4197.
29 X. Liu, P. K. Chu and C. Ding, Surface modification of titanium, titanium alloys and related materials for biomedical applications, *Mater. Sci. Eng., R*, 2004, **47**(3–4), 49–121.
30 Y. M. Wang, D. C. Jia, L. X. Guo, *et al.*, Effect of discharge pulsating on microarc oxidation coatings formed on Ti6Al4V alloy, *Mater. Chem. Phys.*, 2005, **90**(1), 128–133.
31 L. H. Li, Y. M. Kong, H. W. Kim, *et al.*, Improved biological performance of Ti implants due to surface modification by micro-arc oxidation, *Biomaterials*, 2004, **25**(14), 2867–2875.
32 X. Zhu, K. H. Kim and Y. Jeong, Anodic oxide films containing Ca and P of titanium biomaterial, *Biomaterials*, 2001, **22**(16), 2199–2206.
33 X. Zhu, J. L. Ong, S. Kim, *et al.*, Surface characteristics and structure of anodic oxide films containing Ca and P on a titanium implant material, *J. Biomed. Mater. Res.*, 2010, **60**(2), 333–338.
34 L. Muller and F. A. Muller, Preparation of SBF with different HCO_3^- content and its influence on the composition of biomimetic apatites, *Acta Biomater.*, 2006, **2**, 181–189.
35 R. Zhou, D. Wei, S. Cheng, *et al.*, Structure, MC3T3-E1 cell response, and osseointegration of macroporous titanium implants covered by a bioactive microarc oxidation coating with microporous structure, *ACS Appl. Mater. Interfaces*, 2014, **6**(7), 4797–4811.
36 Y. M. Zhang, P. Bataillon-Linez, P. Huang, *et al.*, Surface analyses of micro-arc oxidized and hydrothermally treated titanium and effect on osteoblast behavior, *J. Biomed. Mater. Res., Part A*, 2010, **68**(2), 383–391.
37 R. Rodriguez, K. Kim and J. L. Ong, In vitro osteoblast response to anodized titanium and anodized titanium followed by hydrothermal treatment, *J. Biomed. Mater. Res., Part A*, 2003, **65**(3), 352.
38 F. Liu, F. Wang, T. Shimizu, *et al.*, Hydroxyapatite formation on oxide films containing Ca and P by hydrothermal treatment, *Ceram. Int.*, 2006, **32**(5), 527–531.
39 J. Zhou and Y. Han, Effect of hydrothermal treatment model on the formation of Sr-HA nanorod arrays on microarc oxidized titania coatings, *Appl. Surf. Sci.*, 2013, **286**, 384–390.
40 D. Qing, W. Daqing, W. Shaodong, *et al.*, Rapidly formation of the highly bioactive surface with hydroxyapatite crystals on the titania micro arc oxidation coating by microwave hydrothermal treatment, *Appl. Surf. Sci.*, 2019, **487**(9), 708–718.
41 D. Qing, W. Daqing, W. Shaodong, *et al.*, TEM analysis and in vitro and in vivo biological performance of the hydroxyapatite crystals rapidly formed on the modified

© 2021 The Author(s). Published by the Royal Society of Chemistry

Open Access Article. Published on 12 February 2021. Downloaded on 1/22/2026 6:37:11 AM.
This article is licensed under a Creative Commons Attribution-NonCommercial 3.0 Unported Licence.

microarc oxidation coating using microwave hydrothermal technique, *Chem. Eng. J.*, 2019, **373**(10), 1091–1110.

42 D. Wei, Q. Du, S. Wang, *et al.*, Rapid Fabrication, Microstructure, and In Vitro and In Vivo Investigations of a High-Performance Multilayer Coating with External, Flexible, and Silicon-Doped Hydroxyapatite Nanorods on Titanium, *ACS Biomater. Sci. Eng.*, 2019, **5**(9), 4244–4262.

43 J. Zhou, B. Li, S. Lu, *et al.*, Regulation of Osteoblast Proliferation and Differentiation by Interrod Spacing of Sr-HA Nanorods on Microporous Titania Coatings, *ACS Appl. Mater. Interfaces*, 2013, **5**(11), 5358–5365.

44 R. Zhou, D. Wei, S. Cheng, *et al.*, Structure, MC3T3-E1 cell response, and osseointegration of macroporous titanium implants covered by a bioactive microarc oxidation coating with microporous structure, *ACS Appl. Mater. Interfaces*, 2014, **6**(7), 4797–4811.

45 R. Zhou, D. Wei, J. Cao, *et al.*, Synergistic effects of surface chemistry and topologic structure from modified microarc oxidation coatings on Ti implants for improving osseointegration, *ACS Appl. Mater. Interfaces*, 2015, **7**(16), 8932–8941.

46 R. Zhou, D. Wei, H. Yang, *et al.*, Osseointegration of bioactive microarc oxidized amorphous phase/TiO_2 nanocrystals composited coatings on titanium after implantation into rabbit tibia, *J. Mater. Sci.: Mater. Med.*, 2014, **25**(5), 1307–1318.

47 Y. Han, J. Zhou, L. Zhang, *et al.*, A multi-scaled hybrid orthopedic implant: bone ECM-shaped SrHA nanofibers on the microporous walls of a macroporous titanium scaffold, *Nanotechnology*, 2011, **22**(27), 275603.

48 R. Zhou, D. Wei, J. Cao, *et al.*, The effect of NaOH concentration on the steam-hydrothermally treated bioactive microarc oxidation coatings containing Ca, P, Si and Na on pure Ti surface, *Mater. Sci. Eng., C*, 2015, **49**, 669–680.

49 X. Liu, P. Chu and C. Ding, Surface modification of titanium, titanium alloys, and related materials for biomedical applications, *Mater. Sci. Eng., R*, 2004, **47**(3–4), 49–121.

50 D. Buser, R. K. Schenk, S. Steinemann, *et al.*, Influence of surface characteristics on bone integration of titanium implants. A histomorphometric study in miniature pigs, *J. Biomed. Mater. Res.*, 1991, **25**(7), 889–902.

51 X. Zhu, J. Chen, L. Scheideler, *et al.*, Cellular Reactions of Osteoblasts to Micron- and Submicron-Scale Porous Structures of Titanium Surfaces, *Cells Tissues Organs*, 2004, **178**(1), 13–22.

52 D. Kabaso, E. Gongadze, S. Perutková, *et al.*, Mechanics and electrostatics of the interactions between osteoblasts and titanium surface, *Comput. Methods Biomech. Biomed. Eng.*, 2011, **14**(4–6), 469–482.

53 M. C. Siebers, P. J. T. Brugge, X. F. Walboomers, *et al.*, Integrins as linker proteins between osteoblasts and bone replacing materials. A critical review, *Biomaterials*, 2005, **26**(2), 137–146.

54 Y. W. Lim, S. Y. Kwon, D. H. Sun, H. E. Kim and Y. S. Kim, Enhanced cell integration to titanium alloy by surface treatment with microarc oxidation: a pilot study, *Clin. Orthop. Relat. Res.*, 2009, **467**, 2251–2258.

55 J. Huang, *et al.*, In vitro assessment of the biological response to nano-sized hydroxyapatite, *J. Mater. Sci.: Mater. Med.*, 2004, **15**(4), 441–445.

56 M. López-Alvarez, E. L. Solla, P. González, *et al.*, Silicon-hydroxyapatite bioactive coatings (Si-HA) from diatomaceous earth and silica. Study of adhesion and proliferation of osteoblast-like cells, *J. Mater. Sci.: Mater. Med.*, 2009, **20**(5), 1131.

© 2021 The Author(s). Published by the Royal Society of Chemistry